Mon. Not. R. Astron. Soc. **000**, 1–16 (2002) Printed 28 May 2002 (MN LATEX style file v1.4)

The Sunyaev–Zel'dovich angular power spectrum as a probe of cosmological parameters

E. Komatsu[1]⋆ and U. Seljak[2]†

[1] *Department of Astrophysical Sciences, Princeton University, Princeton, NJ 08544, USA*

[2] *Department of Physics, Princeton University, Princeton, NJ 08544, USA*

28 May 2002

ABSTRACT

The angular power spectrum of the Sunyaev–Zel'dovich (SZ) effect is a powerful probe of cosmology. It is easier to detect than individual clusters in the field, is insensitive to observational selection effects and does not require a calibration between cluster mass and flux, reducing the systematic errors which dominate the cluster-counting constraints. It receives a dominant contribution from virialized cluster region between $20\% - 40\%$ of the virial radius and is thus relatively insensitive to the poorly known gas physics in the cluster centre, such as cooling or (pre)heating. In this paper we derive a refined analytic prediction for the SZ angular power spectrum using the universal gas-density and temperature profile and the dark-matter halo mass function. The predicted power spectrum has no free parameters and fits all of the published hydrodynamic simulation results to better than a factor of two for $l < 10000$. We find that the angular power spectrum C_l scales as $C_l \propto \sigma_8^7 (\Omega_{\rm b} h)^2$ and is almost independent of all of the other cosmological parameters. This differs from the local cluster abundance studies, which give a relation between σ_8 and $\Omega_{\rm m}$. We also compute the covariance matrix of C_l using the halo model and find a good agreement relative to the simulations. We argue that the best constraint from the SZ power spectrum comes from $l \sim 3000$, where the sampling variance is sufficiently small and the spectrum is dominated by massive clusters above $10^{14}\ h^{-1}\ M_\odot$ for which cooling, heating and details of star formation are not very important. We estimate how well we can determine $\sigma_8(\Omega_{\rm b} h)^{2/7}$ with sampling-variance-limited observations and find that for a several-square-degree survey with arcminute resolution one should be able to determine σ_8 to within a few percent, with the remaining uncertainty dominated by theoretical modeling. If the recent excess of the CMB power on small scales reported by the CBI experiment is due to the SZ effect, then we find $\sigma_8(\Omega_{\rm b} h/0.035)^{0.3} = 1.05 \pm 0.15$ at 95% confidence level (statistical) and with a residual 10% systematic (theoretical) uncertainty.

Key words: cosmology: theory — cosmic microwave background — dark matter — galaxies: haloes — galaxies: clusters: general — cosmological parameters

1 INTRODUCTION

Abundance of dark-matter halos and its redshift evolution have been recognized as an important cosmological test. For example, the local abundance of X-ray clusters can be used to constrain a combination of the matter-fluctuation amplitude and the matter density of the universe (e.g., White, Efstathiou, & Frenk 1993; Viana & Liddle 1996; Eke, Cole, & Frenk 1996; Kitayama & Suto 1997). Higher-redshift clusters can be used to break this degeneracy (e.g., Bahcall & Fan 1998), as well as constrain other cosmological parameters (Haiman, Mohr, & Holder 2001).

There are two major uncertainties in such analysis. One is the sample itself, which has to be carefully constructed to avoid any possible selection biases that can affect the final constraint. The other is the relation between observable quantities (e.g., X-ray temperature or flux) and the halo mass, which is related to the theoretical models. The latter uncertainty is particularly important as a small error in this relation can result in a significant effect on the final results. For example, the X-ray flux scales as gas-density squared and is dominated by the central regions, where complicated physical processes are taking place. This means that the relation between flux or flux-weighted temperature and the halo mass is not easily obtained from *ab-initio* numerical simulations, and one must resort to more empirical calibrations instead.

The Sunyaev–Zel'dovich (SZ) effect has some advantages over X-ray in this respect. The SZ effect is caused by the cosmic microwave background (CMB) photons scattering off hot electrons

⋆ E-mail: komatsu@astro.princeton.edu

† E-mail: useljak@princeton.edu

in the intracluster medium, and the SZ flux is proportional to the projected electron-gas pressure, which is proportional to a product of electron number density and temperature along the line of sight. Relative to X-ray emission this has a larger contribution from the outer parts of the cluster, where the missing physics such as gas preheating or cooling in numerical simulations is less significant.

However, the SZ effect is very difficult to measure and currently only detections of already-known clusters exist (Birkinshaw 1999). It is likely that the first SZ detection in a random direction will not be that of a specific cluster, but of a field correlation function, or the angular power spectrum C_l, with several low signal-to-noise clusters contributing to the signal. Even if individual clusters are too faint to be detected with high statistical significance, the combined effect in C_l can be statistically significant. There have been several observational efforts in measuring the small-scale fluctuations, and upper-limits have been obtained by ATCA (Subrahmanyan et al. 1998), BIMA (Holzapfel et al. 2000; Dawson et al. 2001), SUZIE (Church et al. 1997; Ganga et al. 1997), and VLA (Partridge et al. 1997). Recently, CBI has reported statistically significant detection of the small-scale fluctuations at the level of 20 μK on arcminutes angular scales (Mason et al. 2002), and their result may already be providing the first detection of the SZ fluctuations (Bond et al. 2002).

There are other advantages of using power spectrum in addition to the higher statistical significance in a noisy map. One is that selection effects are less important than in a cluster survey, for which flux, surface brightness, and other selection criteria have to be carefully examined to avoid any biases. The other is that we do not have to measure the mass of individual haloes. As discussed above this is a dominant source of uncertainty in the local-mass-function determination from X-ray clusters and lack of a good calibration can lead to a 30% error on σ_8. Even if mass were determined from SZ flux, for which the central regions are less important, one would still need to include effects such as substructure, projections, ellipticity etc. As we argue in this paper using the SZ power spectrum instead of the number-count analysis is less sensitive to selection biases and can still give statistically significant results. It is true that the power spectrum does not use all of the information available, specially if one obtains the information on cluster redshifts. However, the SZ power spectrum provides quite powerful constraints on cosmological parameters already by itself and the small increase in statistical errors is more than compensated by the decrease in the systematic uncertainties. Thus initial experimental efforts should focus on the power spectrum as a more reliable method to determine the cosmological parameters.

There are of course other effects that contribute to fluctuations in this range of wavelengths. The SZ effect is the dominant contribution for $l > 2000 - 4000$, depending on its amplitude. The primary CMB dominates on the larger scales. Although the primary CMB confuses the SZ effect, we can reduce or eliminate it by observing at 217 GHz at which the SZ effect vanishes. Many of the current generation CMB experiments (such as CBI) operate at low frequencies, where the frequency dependence of CMB and the SZ effect is similar, and the two cannot be distinguished very well on this basis. Galactic emission (synchrotron, dust, or free-free) does not have much power on the small angular scales, and has a different frequency dependence from CMB. They are not likely to be a major source of contamination.

Point sources have a lot of small-scale power and are potentially more problematic contaminant. While we can easily identify bright (more than several-σ) point sources, we cannot identify the fainter ones, which will contaminate the SZ effect. This is particularly problematic for narrow frequency coverage experiments such as CBI, as we cannot use different frequency dependence of the point sources to separate the two components. We can still try to use opposite signatures between SZ and point sources as a way to distinguish them; the SZ effect is negative in flux at low frequencies, while point sources are positive. This results in a skewed one-point-distribution function. We can also use the difference in the shape of the correlation function, since more extended correlation in the SZ effect differs from the point sources. The SZ power spectrum scales roughly as l^{-2} while that of the point sources is constant, so the two can be distinguished. In practice noise and beam smoothing may make this analysis more complicated.

Within a few years, several experiments will likely measure the SZ effect with an arcminute angular resolution and the effective area of several square degrees. This has motivated us to revisit the predictions for the SZ angular power spectrum. Many analytic calculations exist in the literature (Cole & Kaiser 1988; Makino & Suto 1993; Atrio-Barandela & Mücket 1999; Komatsu & Kitayama 1999; Cooray 2000; Molnar & Birkinshaw 2000; Holder & Carlstrom 2001; Zhang & Pen 2001), as well as many hydrodynamic-simulation results (Scaramella, Cen, & Ostriker 1993; Persi et al. 1995; Refregier et al. 2000; Seljak, Burwell, & Pen 2001; da Silva et al. 2000; da Silva et al. 2001a; da Silva et al. 2001b; Springel, White, & Hernquist 2001; Refregier & Teyssier 2000; Zhang, Pen, & Wang 2002). The comparison between different simulations is difficult, as the parameters used differ, and the resulting power spectrum is extremely sensitive to the chosen parameters. Since massive clusters are at the tail of the dark-matter mass function, the r.m.s. mass fluctuations within a 8 h^{-1} Mpc sphere, σ_8, is the most important parameter among the cosmological parameters. Komatsu & Kitayama (1999) have shown that the matter density of the universe is less important than σ_8.

Refregier et al. (2000) and Refregier & Teyssier (2000) have attempted to compare analytic predictions based upon the so-called "halo approach" (section 2) with their simulated power spectrum, finding a good agreement. This agreement is, however, partially built into their model; in their approach, the parameters such as upper and lower mass cut-off are chosen to agree with the simulations. Another free parameter used in the analytic modeling that cannot be obtained from these models is the mass–temperature normalization. Although a virial relation has often been used in this context, the overall amplitude is treated as a free parameter, and cannot be justified without a more detailed model. In this paper we develop a more refined analytic model and show that it reproduces the simulation results without any free parameters, at least at the level of the simulations disagreeing among themselves.

The main ingredients into the halo model are the dark-matter-halo mass function, the gas-density and the gas-temperature profiles. For the latter, we use an analytic gas and temperature profile model developed in our previous paper (Komatsu & Seljak 2001). We have shown that it reproduces well the simulation results in the outer parts of the cluster which are relevant for the SZ effect. This model fixes the normalization between mass and temperature by requiring that the gas and the dark-matter profiles agree with each other outside the gas core. Hydrodynamic simulations (e.g., Frenk et al. 1999) have shown that this assumption holds accurately. As a result of this assumption and hydrostatic equilibrium the gas temperature declines in the outer parts of the cluster, which is also seen in the simulations (although it remains controversial in X-ray observations due to the faint levels of X-ray emission in the outer parts of the cluster). This model therefore reproduces the main features of the hydrodynamic simulations and can be viewed as the gas analog of the often-used NFW profile (Navarro, Frenk, & White 1997) for dark matter, at least outside the gas core where additional physics may play a role.

The structure of this paper is as follows. In § 2 we outline the "halo approach" to calculating the SZ angular power spectrum. In § 3 we derive the universal gas-density, gas-temperature, and gas-pressure profiles following the prescription described by Komatsu & Seljak (2001). In § 4 we predict the spectrum and compare it to the hydrodynamic simulations. We then investigate the dependence of the spectrum on various cosmological parameters. We also study the mass and redshift distribution of the spectrum. In § 5 we compute the covariance matrix of C_l by taking into account non-Gaussianity of the SZ fluctuations and compare these to the hydrodynamic simulations. In § 6 we show how well we can determine σ_8 with realistic SZ observations using a likelihood analysis. We put constraints on a $\Omega_{\rm m} - \sigma_8$ plane using the recent CBI data of the small-scale CMB fluctuations at $l > 1500$ (Mason et al. 2002). In § 7 we quantify the theoretical uncertainty in our predictions. Finally, we summarize our results in § 8. The fiducial cosmological model in this paper is $\Omega_{\rm m} = 0.37$, $\Omega_\Lambda = 0.63$, $\Omega_{\rm b} = 0.05$, $h = 0.7$, $w = -1.0$, $n = 1.0$, and $\sigma_8 = 1.0$.

2 HALO APPROACH TO THE SZ ANGULAR POWER SPECTRUM

To compute the angular power spectrum of the SZ effect we use the halo formalism (Cole & Kaiser 1988; Makino & Suto 1993; Atrio-Barandela & Mücket 1999; Komatsu & Kitayama 1999; Cooray 2000; Molnar & Birkinshaw 2000; Holder & Carlstrom 2001). For the angular scales of interest here, $l > 300$, the one-halo Poisson term dominates C_l even after the subtraction of local massive haloes (Komatsu & Kitayama 1999). We thus neglect the halo-halo correlation term throughout the paper.

The expression for C_l is given by

$$C_l = g_\nu^2 \int_0^{z_{\max}} dz \frac{dV}{dz} \int_{M_{\min}}^{M_{\max}} dM \frac{dn(M,z)}{dM} \left|\tilde{y}_l(M,z)\right|^2, \quad (1)$$

where g_ν is the spectral function of the SZ effect (-2 in the Rayleigh–Jeans limit) (Sunyaev & Zeldovich 1980), $V(z)$ the comoving volume of the universe at z per steradian, $dn(M,z)/dM$ the comoving dark-matter-halo mass function, and $\tilde{y}_l(M,z)$ the 2D Fourier transform of the projected Compton y-parameter. The virial mass M used here and its mass function are described in more detail in section 2.1.

For the upper integration boundary of redshift it suffices to take $z_{\max} = 10$ (figure 5). For the mass integration boundaries, $M_{\min}$ and $M_{\max}$, we find that $M_{\min} = 5\times10^{11}\ h^{-1}\ M_\odot$ and $M_{\max} = 5\times10^{15}\ h^{-1}\ M_\odot$ suffice to get the integral to converge on all angular scales, whereas $M_{\min} = 5\times10^{12}\ h^{-1}\ M_\odot$ is sufficient for $l < 10^4$ (figure 6). Since the integrals converge the results are not subject to the specific choice of integration boundaries.

The 2D Fourier transform of the projected Compton y-parameter, $\tilde{y}_l = \tilde{y}_l(M,z)$, is given by

$$\tilde{y}_l = \frac{4\pi r_{\rm s}}{l_{\rm s}^2} \int_0^\infty dx x^2 y_{\rm 3D}(x) \frac{\sin(lx/l_{\rm s})}{lx/l_{\rm s}}, \quad (2)$$

where $y_{\rm 3D}(x)$ is the 3D radial profile of the Compton y-parameter (equation 7 in section 3). Note that $y_{\rm 3D}(x)$ has a dimension of $(\mathrm{length})^{-1}$, while $\tilde{y}_l$ is dimensionless. In equation (2) we have used x as a scaled, non-dimensional radius,

$$x \equiv r/r_{\rm s}, \quad (3)$$

where $r_{\rm s} = r_{\rm s}(M,z)$ is a scale radius which characterizes the 3D radial profile and the corresponding angular wave number is

$$l_{\rm s} \equiv d_{\rm A}/r_{\rm s}. \quad (4)$$

Here $d_{\rm A} = d_{\rm A}(z)$ is the proper angular-diameter distance. The projection of the 3D profile onto the sky in equation (2) was done within the Limber's approximation. In section 3, we derive $y_{\rm 3D}(x)$ using the universal gas and temperature profile.

2.1 Dark-matter halo mass function

For the dark-matter halo mass function $dn(M,z)/dM$ in equation (1) we use the universal mass function (Jenkins et al. 2001), which was derived from N-body simulations. We should be careful about the definition of "mass" when using the mass function derived from N-body simulations (e.g., White 2001; Seljak 2001; Hu & Kravtsov 2002). The mass of haloes in the simulations is usually not the virial mass M as defined in our analytic formulation (equation 1). Instead, the simulations usually use either the friend-of-friend (FOF) mass or the spherical overdensity (SO) mass to define the haloes. We use here the SO mass, as the FOF mass is difficult to interpret in the context of analytic formulation.

We define the SO mass, M_δ, as the mass within the spherical region whose density is δ times the critical density of the universe at z $\rho_{\rm c}(z)$ (note that sometimes one uses instead the mass within the spherical region whose density is $\tilde{\delta}$ times the mean mass density of the universe at z, $\rho_{\rm m}(z) = \Omega_{\rm m}(z)\rho_{\rm c}(z)$; the two are related through $\delta = \Omega_{\rm m}(z)\tilde{\delta}$). Since N-body simulations give $dn(M_\delta,z)/dM_\delta$, we need to convert it into $dn(M,z)/dM$. We do this by calculating

$$\frac{dn(M,z)}{dM} = \frac{dM_\delta}{dM}\frac{dn(M_\delta,z)}{dM_\delta}. \quad (5)$$

For a given virial mass, M, we calculate M_δ with equation (14) of Komatsu & Seljak (2001), and also evaluate dM_δ/dM numerically.

We use equation (B3) of Jenkins et al. (2001), which explicitly uses $\delta = 180\Omega_{\rm m}(z)$ (mass density of haloes is 180 times the mean mass density of the universe at z),

$$\begin{aligned}\frac{dn(M_\delta,z)}{dM_\delta} &= \Omega_{\rm m}(0)\frac{\rho_{\rm c}(0)}{M_\delta}\frac{d\ln\sigma^{-1}}{dM_\delta} \\ &\quad \times 0.301\exp\left(-\left|\ln\sigma^{-1}+0.64\right|^{3.82}\right), \end{aligned} \quad (6)$$

where $\sigma = \sigma(M_\delta,z)$ is the linear, r.m.s. mass fluctuations at a given redshift z within the top-hat filter. To compute σ we use the BBKS transfer function (Bardeen et al. 1986) with the baryonic correction made by Sugiyama (1995). The present-day critical density of the universe is $\rho_{\rm c}(0) = 2.775\times10^{11}\ h^2\ M_\odot\ \mathrm{Mpc}^{-3}$. Note that we have defined the mass function as the comoving number density.

While the functional formula for the mass function in equation (6) was tested for just one cosmological model (τCDM model) by Jenkins et al. (2001), it is essentially a non-smoothed version of their universal mass function valid for a broad range of models. Hu & Kravtsov (2002) have shown that the formula agrees with their simulated mass function as well which uses a different cosmological model. In addition, Evrard et al. (2001) have shown that their mass function for the SO mass haloes with $\delta = 200$ agrees with the Jenkins et al.'s formula, once taking into account the mass definition properly (see also related discussion in Seljak 2001 and Hu &

Kravtsov 2002). There is thus increasing evidence for the accuracy of Jenkins et al.'s mass function.

3 GAS-PRESSURE PROFILE OF HALOES

3.1 Introduction

The 3D Compton y-parameter profile, $y_{3\mathrm{D}}(x)$, is given by a thermal gas-pressure profile, $P_{\mathrm{gas}}(x)$, through

$$\begin{aligned} y_{3\mathrm{D}}(x) &\equiv \frac{\sigma_{\mathrm{T}}}{m_e c^2} P_e(x) = \frac{\sigma_{\mathrm{T}}}{m_e c^2}\left(\frac{2+2X}{3+5X}\right) P_{\mathrm{gas}}(x) \\ &= 1.04\times 10^{-4}\ \mathrm{Mpc}^{-1}\left[\frac{P_{\mathrm{gas}}(x)}{50\ \mathrm{eV\ cm}^{-3}}\right], \end{aligned} \tag{7}$$

where $P_e(x)$ is an electron-pressure profile, $X = 0.76$ the primordial hydrogen abundance, σ_{T} the Thomson cross section, m_e the electron mass, and c the speed of light.

We may write $P_{\mathrm{gas}}(x)$ with a gas-density profile, $\rho_{\mathrm{gas}}(x)$, and a gas-temperature profile, $T_{\mathrm{gas}}(x)$, as

$$\begin{aligned} P_{\mathrm{gas}}(x) &= \frac{3+5X}{4}\frac{\rho_{\mathrm{gas}}(x)}{m_p} k_{\mathrm{B}} T_{\mathrm{gas}}(x) \\ &= 55.0\ \mathrm{eV\ cm}^{-3} \\ &\quad\times\left[\frac{\rho_{\mathrm{gas}}(x)}{10^{14}\ M_\odot\ \mathrm{Mpc}^{-3}}\right]\left[\frac{k_{\mathrm{B}} T_{\mathrm{gas}}(x)}{8\ \mathrm{keV}}\right], \end{aligned} \tag{8}$$

where m_p is the proton mass, and k_{B} the Boltzmann constant.

The aim of this section is to derive $P_{\mathrm{gas}}(x)$ following Komatsu & Seljak (2001). Pressure profile was one of the uncertainties in the previous work on the SZ power spectrum: most of the previous work uses a spherical-isothermal β model as a gas-density profile, with β fixed at $2/3$ for simplicity (Makino & Suto 1993; Atrio-Barandela & Mücket 1999; Komatsu & Kitayama 1999; Molnar & Birkinshaw 2000; Holder & Carlstrom 2001); Cooray (2000) used an isothermal gas-density profile as predicted by Makino, Sasaki, & Suto (1998), which uses hydrostatic equilibrium between gas pressure and dark-matter potential, and is close to the β profile. The β profile does not, however, reproduce the simulation results in the outer parts of the haloes. The outer slope of the β model with $\beta = 2/3$ scales as r^{-2}, being significantly shallower than the gas profile in simulations which, as we have argued, is similar to the dark-matter profile and asymptotically scales as r^{-3}. Since the SZ effect is sensitive to the outer parts of haloes, this can cause a significant error in the predictions.

There is a related uncertainty caused by the shallow (r^{-2}) profile: one has to cut out the extension of gas in haloes at an arbitrary radius, otherwise one predicts too much power on large angular scales. We find that the previous predictions are unstable against this cut-off radius. This radius, which is a free parameter, has been assumed to be the virial radius; however, for isothermal gas assumed in the previous work this is *ad hoc*, as neither temperature nor density profile shows the abrupt cut-off at the virial radius in hydrodynamic simulations (Bryan & Norman 1998; Eke, Navarro, & Frenk 1998; Frenk et al. 1999). Instead, both the temperature and the density decrease smoothly across the virial radius, and it is only at $2-3$ times the virial radius that there seems to be an abrupt decrease of the temperature to the IGM value, the so-called shock radius (Bryan & Norman 1998).

Once the decline in profiles relative to the β model is included, the contribution from the outer parts of haloes to the SZ power spectrum converges well within the shock radius, and is thus independent of the outer cut-off of the profile. This is because requiring that the gas-density profile traces the dark-matter-density profile leads to $\rho_{\mathrm{gas}} \propto r^{-3}$ in the outer parts of the haloes. This by itself would give a logarithmically divergent gas-mass profile; however, since the temperature is also declining with radius, the resulting pressure profile is convergent. Hydrostatic equilibrium and the gas density tracing the dark-matter density make the gas temperature decrease with radius.

3.2 Universal dark-matter-density profile

The universal NFW dark-matter-density profile (Navarro, Frenk, & White 1997) is

$$\rho_{\mathrm{dm}}(x) = \frac{\rho_{\mathrm{s}}}{x(1+x)^2}, \tag{9}$$

where $x \equiv r/r_{\mathrm{s}}$, r_{s} a scale radius, and ρ_{s} a scale density. While the exact shape in the inner parts is still uncertain (Moore et al. 1998; Jing & Suto 2000; Klypin et al. 2001), it does not affect the SZ effect, given the scales of interest here.

To specify the NFW profile, we need to specify a scale radius, r_{s}, as a function of mass and redshift. It is customary to specify the concentration parameter c instead of r_{s},

$$c(M,z) \equiv \frac{r_{\mathrm{vir}}(M,z)}{r_{\mathrm{s}}(M,z)} \approx \frac{10}{1+z}\left[\frac{M}{M_*(0)}\right]^{-0.2}, \tag{10}$$

where $r_{\mathrm{vir}}(M,z)$ is the virial radius of haloes, and the last expression follows from Seljak (2000) with redshift evolution found by Bullock et al. (2001). The "non-linear mass" at $z=0$, $M_*(0)$, is a solution to $\sigma(M) = \delta_c$, where $\sigma(M)$ is the present-day r.m.s. mass fluctuations within the top-hat filter, M the virial mass, and δ_c the threshold overdensity of spherical collapse at $z=0$ (Lacey & Cole 1993; Nakamura & Suto 1997). We calculate the virial radius using the spherical collapse model,

$$r_{\mathrm{vir}}(M,z) \equiv \left[\frac{M}{(4\pi/3)\Delta_{\mathrm{c}}(z)\rho_{\mathrm{c}}(z)}\right]^{1/3}, \tag{11}$$

where $\Delta_{\mathrm{c}}(z)$ is a spherical overdensity of the virialized halo within r_{vir} at z, in units of the critical density of the universe at z (Lacey & Cole 1993; Nakamura & Suto 1997).

The exact form of $c(M,z)$, equation (10), is somewhat uncertain. There are various fitting formulae in the literature (Navarro, Frenk, & White 1997; Eke, Navarro, & Steinmetz 2001; Bullock et al. 2001; Seljak 2000; Cooray, Hu, & Miralda-Escudé 2000). In section 4 we study the effect of different concentration parameters on our predictions, in addition to using our fiducial concentration parameter dependence in equation (10). We find that the difference in concentration parameters does not affect our predictions, largely because the SZ effect is not sensitive to the central parts of haloes, where the profile shape makes most difference.

3.3 Universal gas-pressure profile

To derive a gas-pressure profile $P_{\mathrm{gas}}(x)$ we make three assumptions: (1) hydrostatic equilibrium between gas pressure and dark-matter potential due to the universal dark-matter density profile, (2) gas density tracing the universal dark-matter density in the outer parts of haloes, and (3) a constant polytropic equation of state for gas, $P_{\mathrm{gas}} \propto \rho_{\mathrm{gas}}^{\gamma}$. The assumption (3) is obviously just an approximation and can be justified only to the extent that it suffices to explain the observations or simulations. There is evidence for this assumption to fail within inner 5% of the virial radius, where X-ray observations indicate that temperature increases with radius (Allen, Schmidt, & Fabian 2001). Outside the core region, nevertheless, the constant polytropic index seems to suffice, at least in comparison to the simulations.

From these three assumptions one can obtain universal gas-density, gas-temperature, and gas-pressure profiles as

$$\rho_{\rm gas}(x) = \rho_{\rm gas}(0) y_{\rm gas}(x), \tag{12}$$

$$T_{\rm gas}(x) = T_{\rm gas}(0) y_{\rm gas}^{\gamma-1}(x), \tag{13}$$

and

$$P_{\rm gas}(x) = P_{\rm gas}(0) y_{\rm gas}^{\gamma}(x). \tag{14}$$

Solving the hydrostatic equilibrium equation with the *ansatz* above, we find that the non-dimensional gas-density profile, $y_{\rm gas}(x)$, has an analytic solution, and is given by (Komatsu & Seljak 2001)

$$y_{\rm gas}(x) \equiv \left\{1 - B\left[1 - \frac{\ln(1+x)}{x}\right]\right\}^{1/(\gamma-1)}, \tag{15}$$

where the coefficient B is

$$B \equiv 3\eta^{-1}(0)\frac{\gamma-1}{\gamma}\left[\frac{\ln(1+c)}{c} - \frac{1}{1+c}\right]^{-1}. \tag{16}$$

In appendix, we give exact formulae for the polytropic index, γ, and the mass–temperature normalization factor at the centre, $\eta(0)$. Here we provide instead useful fitting formulae:

$$\gamma = 1.137 + 8.94\times 10^{-2}\ln(c/5) - 3.68\times 10^{-3}(c-5), \tag{17}$$

and

$$\eta(0) = 2.235 + 0.202(c-5) - 1.16\times 10^{-3}(c-5)^2. \tag{18}$$

These fitting formulae are valid for $1 < c < 25$. Since $\gamma > 1$ and the density decreases with radius, the temperature also decreases with radius.

From $\eta(0)$, we can determine the central temperature, $T_{\rm gas}(0)$, as

$$\begin{aligned} T_{\rm gas}(0) &= \eta(0)\frac{4}{3+5X}\frac{Gm_pM}{3r_{\rm vir}} \\ &= 8.80\ {\rm keV}\ \eta(0)\left[\frac{M/(10^{15}\ h^{-1}\ M_\odot)}{r_{\rm vir}/(1\ h^{-1}\ {\rm Mpc})}\right]. \end{aligned} \tag{19}$$

The central gas density, $\rho_{\rm gas}(0)$, is determined by equation (21) below. We then compute the central gas pressure, $P_{\rm gas}(0)$, by substituting $\rho_{\rm gas}(0)$ and $T_{\rm gas}(0)$ into equation (8). This completely specifies the gas-density, the gas-temperature, and the gas-pressure profiles of haloes and their normalizations.

We determine the amount of gas in haloes by requiring that the gas density in the outer parts of haloes is $\Omega_{\rm b}/\Omega_{\rm m}$ times the dark-matter density. Unlike the β profile this is self-consistent, as our gas-density profile agrees with the dark-matter profile outside the gas core. The virial radius thus has no special importance, and the matching can be performed over a broad range of radii without affecting the results. We should reduce the gas fraction by the amount that has been converted to stars, which is of order $10\% - 20\%$ for massive clusters of interest here (Fukugita, Hogan, & Peebles 1998). We choose not to apply this correction, so our predictions for the power spectrum are somewhat overestimated and the corresponding amplitude constraints underestimated. This however translates into only a few percent correction to the amplitude of σ_8.

We normalize the gas density at the virial radius,

$$\begin{aligned} \rho_{\rm gas}(c) &= \rho_{\rm gas}(0)y_{\rm gas}(c) = \frac{\Omega_{\rm b}}{\Omega_{\rm m}}\rho_{\rm dm}(c) \\ &= \frac{\Omega_{\rm b}}{\Omega_{\rm m}}\frac{M}{4\pi r_{\rm vir}^3}\frac{c^2}{(1+c)^2}\left[\ln(1+c) - \frac{c}{1+c}\right]^{-1}. \end{aligned} \tag{20}$$

We use this equation to obtain the central gas density,

$$\begin{aligned} \rho_{\rm gas}(0) &= 7.96\times 10^{13}\ M_\odot\ {\rm Mpc}^{-3} \\ &\times \left(\frac{\Omega_{\rm b}h^2}{\Omega_{\rm m}}\right)\frac{M/(10^{15}\ h^{-1}\ M_\odot)}{[r_{\rm vir}/(1\ h^{-1}\ {\rm Mpc})]^3} \\ &\times c^3\left[\frac{y_{\rm gas}^{-1}(c)}{c^2(1+c)^2}\right]\left[\ln(1+c) - \frac{c}{1+c}\right]^{-1}, \end{aligned} \tag{21}$$

or equivalently

$$\begin{aligned} \rho_{\rm gas}(0) &= 2.55\times 10^{14}\ M_\odot\ {\rm Mpc}^{-3} \\ &\times \left(\frac{\Omega_{\rm b}h^2/\Omega_{\rm m}}{0.05}\right)\frac{M/(10^{15}\ h^{-1}\ M_\odot)}{[r_{\rm s}/(0.25\ h^{-1}\ {\rm Mpc})]^3} \\ &\times \left[\frac{y_{\rm gas}^{-1}(c)}{c^2(1+c)^2}\right]\left[\ln(1+c) - \frac{c}{1+c}\right]^{-1}. \end{aligned} \tag{22}$$

4 PREDICTIONS FOR THE SZ ANGULAR POWER SPECTRUM

In this section, we predict the SZ angular power spectrum, C_l, by integrating equation (1), and compare the predictions with hydrodynamic simulations. We then study the sensitivity of C_l to various cosmological parameters. We also study mass and redshift distribution of C_l, finding that the power spectrum primarily probes massive haloes in a moderate redshift universe.

4.1 Comparison with hydrodynamic simulations

We begin by comparing our predictions for C_l with six hydrodynamic simulations (four independent codes), listed in table 1. Figure 1 compares our analytic predictions with the simulated power spectra.

The predictions generally agree with the simulations within a factor of two. We find the best agreement for the nominally highest-resolution (512^3) simulation run by Zhang, Pen, & Wang (2002) using mesh-based MMH code (bottom-left panel of figure 1). The same code, but for different cosmological parameters and at lower (256^3) resolution, agrees well below $l < 10000$, but lacks power above that (Seljak, Burwell, & Pen 2001) (top-left panel). Note that the number of realizations for this simulation was small, which explains lack of power at low l compared to even lower (128^3) resolution used by Refregier et al. (2000) for the same code and the same cosmological parameters.

We have rerun the 256^3 simulation with more realizations, covering the effective area of 1000 square degrees. We find that with more realizations C_l at low l increases, being in agreement with Refregier et al. (2000). This indicates that the sampling variance is very large on large scales, but is significantly reduced above $l \sim 2000 - 3000$. With more realizations, one typically increases power on large scales, which explains some of the differences among different simulations (they differ in the effective simulated area significantly; see table 1). At least for MMH code, we find that the numerical resolution seems to be important at high l, and it causes some of the discrepancy between our model and the MMH simulations.

The comparison with one of the two SPH simulations, da Silva et al. (2001b) using HYDRA code, shows a good agreement in shape, while the GADGET code (Springel, White, &

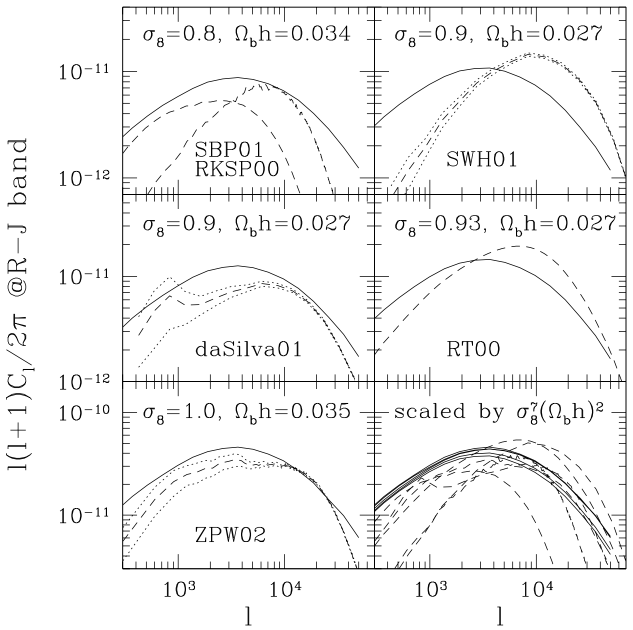

Figure 1. Comparison between the predicted SZ angular power spectra (solid) and the simulations (dashed; see table 1 for the meaning of the labels shown in each panel, and for the cosmological parameters used). The dotted lines indicate r.m.s. errors of the simulated power spectra. The bottom-right panel scales all the power spectra by $\sigma_8^7\,(\Omega_b h)^2$. The agreement between the scaled power spectra indicates that this combination of cosmological parameters controls the amplitude of C_l.

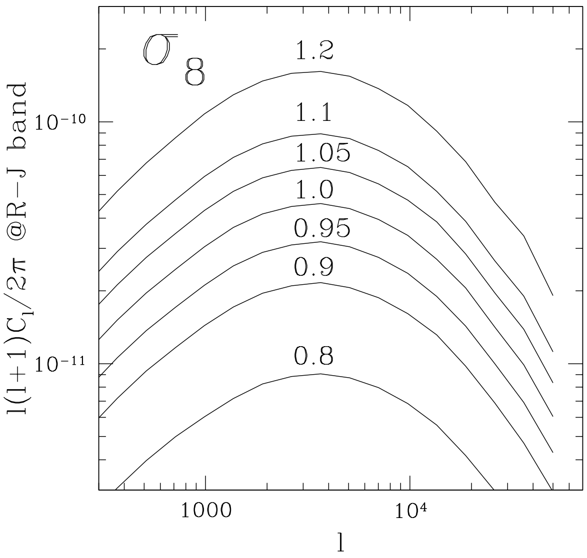

Figure 2. Dependence of the SZ angular power spectrum on σ_8. From top to bottom, the lines indicate $\sigma_8 = 1.2$, 1.1, 1.05, 1.0, 0.95, 0.9, and 0.8, as shown in the figure.

Hernquist 2001) seems to predict more small-scale power above $l \sim 5000$ compared to our predictions. We find that the shape of C_l of Springel, White, & Hernquist (2001) is similar to Refregier & Teyssier (2000), which uses a mesh-based hydrodynamic code, RAMSES, so the disagreement is unlikely to be due to simply SPH versus mesh-based codes. We note that the SPH simulation presented in Bond et al. (2002) also agrees in shape with Springel, White, & Hernquist (2001).

One possible explanation for the discrepancy is that some simulations such as MMH have not yet converged for very high l, while for low l sampling variance seems to be most likely explanation. The discrepancy between our analytic model and GADGET and RAMSES could be caused by failure of our model at high l: clusters at higher redshift are less regular with more merging and substructure, which boosts C_l at high l. One way to account for this in analytic model would be to include subhalos within halos, but to properly calibrate this one would need to use hydrodynamic simulations. Here we argue that around $l \sim 3000$ the theoretical model and the simulations seem to agree rather well, certainly within a factor of two or better. Any remaining discrepancy at low l could be due to insufficient sampling in simulations. Although a factor of two may sound like a large uncertainty in the C_l prediction, it translates into a rather small uncertainty in σ_8, as discussed below.

4.2 Dependence on cosmological parameters

In previous work it has been argued that the SZ power spectrum is very sensitive to σ_8 (Komatsu & Kitayama 1999; Seljak, Burwell, & Pen 2001; Zhang & Pen 2001; Zhang, Pen, & Wang 2002). Figure 2 shows this dependence within the analytic model. For example, a 40% change in σ_8 causes one order of magnitude change in C_l, while a 10% change in σ_8 causes a factor of two change. We find that $C_l \propto \sigma_8^7$ provides a good description of this scaling (see also the bottom-right panel of figure 1). The strong dependence of C_l on σ_8 indicates that even if the numerical simulations are uncertain at the level of a factor of two, this translates into less than 10% systematic uncertainty in σ_8.

This property of the SZ power spectrum should be compared with the current uncertainty in σ_8 from the local cluster abundance studies, for which the systematic uncertainty is larger than 10% because of the uncertainty in the mass–temperature relation (e.g., Pierpaoli, Scott, & White 2001; Seljak 2001; Viana, Nichol, & Liddle 2002). Weak lensing (e.g., Van Waerbeke et al. 2002) and direct mass–temperature calibration may soon provide a more reliable method to determine $\sigma_8\Omega_m^{0.5}$ combination. On the other hand, we show below that C_l is not sensitive to Ω_m in the range of current interest. This property can break the degeneracy between the two parameters.

Figure 3 shows dependence of C_l on Ω_m assuming a flat universe, i.e., $\Omega_\Lambda = 1 - \Omega_m$. While $C_l \propto \Omega_m$ for $\Omega_m > 0.4$, we find that it is almost independent of Ω_m for $0.15 < \Omega_m < 0.4$. This is because the comoving volume of the universe increases rapidly with Ω_m decreasing in this region, canceling out the effect of Ω_m on the dark-matter mass function. As this range of Ω_m is favored by current observations, C_l is practically independent of Ω_m.

Figure 4 shows dependence of C_l on equation of state w, Ω_b, h, and n. While varying Ω_b or h, we have fixed $\Omega_b h$ at a fiducial value, 0.035, since we know that C_l scales as $(\Omega_b h)^2$. The figure shows any residual dependence of C_l on Ω_b or h. We find that C_l depends upon w, Ω_b, h, or n very weakly compared to σ_8 (compare figure 4 with figure 2). The only exception is if $w > -2/3$, which is however not favored by current observations (Bean & Melchiorri 2002).

We find that the dependence of overall amplitude of C_l on cos-

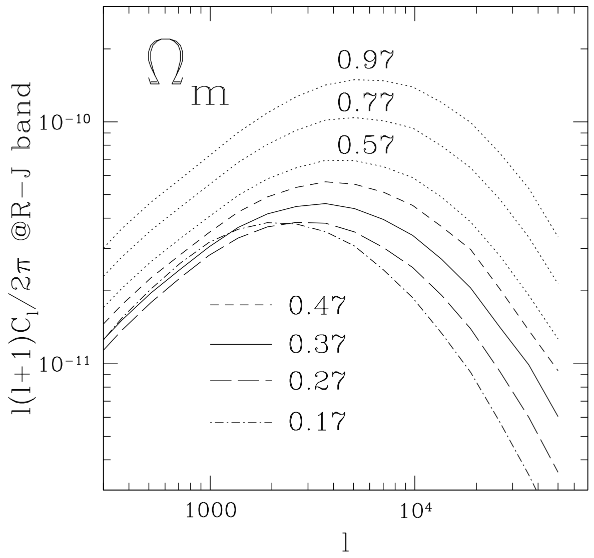

Figure 3. Dependence of the SZ angular power spectrum on $\Omega_{\rm m}$. From top to bottom, the lines indicate $\Omega_{\rm m} = 0.97$, 0.77, 0.57, 0.47, 0.37, 0.27, and 0.17, as shown in the figure. While varying $\Omega_{\rm m}$, we have assumed a flat universe, i.e., $\Omega_\Lambda = 1 - \Omega_{\rm m}$, and $w = -1.0$.

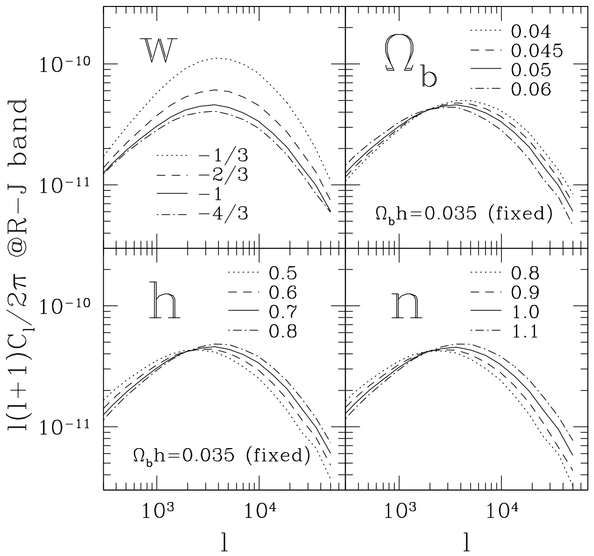

Figure 4. Dependence of the SZ angular power spectrum on the equation of state of the dark-energy component, w, the baryon density $\Omega_{\rm b}$, the Hubble constant in units of 100 km s^{-1} Mpc^{-1}, h, and the primordial power-spectrum slope n. Values of each parameter are shown in each panel of the figure. While varying $\Omega_{\rm b}$ or h, we have $\Omega_{\rm b}h = 0.035$ fixed. The panels for $\Omega_{\rm b}$ and h are to show any residual dependence of C_l on these two parameters. This figure is to be compared with figure 2, showing how insensitive C_l is to w, $\Omega_{\rm b}$, h, or n compared to σ_8.

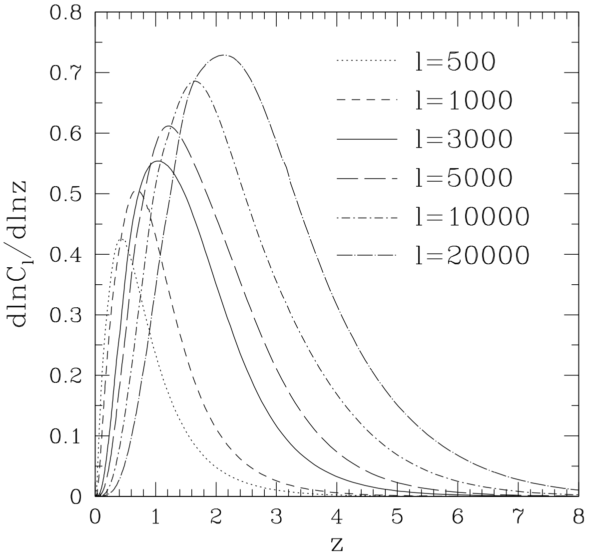

Figure 5. Redshift distribution of C_l. We plot $d\ln C_l/d\ln z$, equation (25), for a given l. From left to right it is shown l = 500, 1000, 3000, 5000, 10000, and 20000, as indicated in the figure.

mological parameters for $0.15 < \Omega_{\rm m} < 0.4$ is well approximated by

$$\frac{l(l+1)C_l}{2\pi} \simeq 330\,\mu{\rm K}^2\,\sigma_8^7\left(\frac{\Omega_{\rm b}h}{0.035}\right)^2 \qquad (0.15 < \Omega_{\rm m} < 0.4)\,, \quad (23)$$

at the peak around $l \sim 4000$. As we have shown in figure 3, C_l is rather insensitive to $\Omega_{\rm m}$ over this region. A fit for $\Omega_{\rm m} > 0.4$ is given by

$$C_l \propto (\Omega_{\rm b}h)^2\,\Omega_{\rm m}\sigma_8^{6.5\Omega_{\rm m}^{-0.2}-0.9\sigma_8} \qquad (\Omega_{\rm m} > 0.4)\,. \quad (24)$$

4.3 Redshift and mass distribution

Figure 5 shows the redshift distribution of C_l for a given l,

$$\frac{d\ln C_l}{d\ln z} \equiv \frac{z\frac{dV}{dz}\int dM\,\frac{dn(M,z)}{dM}\,|\tilde{y}_l(M,z)|^2}{\int dz\frac{dV}{dz}\int dM\,\frac{dn(M,z)}{dM}\,|\tilde{y}_l(M,z)|^2}. \quad (25)$$

We find that haloes at $z \sim 1$ determine C_l at $l \sim 3000$ (angular scales around $3'$). Haloes at $z \sim 2$ dominate C_l at $l = 10000$. Even haloes at $z \sim 3$ have a non-negligible contribution to C_l for $l > 10000$.

Figure 6 shows the mass distribution of C_l for a given l,

$$\frac{d\ln C_l}{d\ln M} \equiv \frac{M\int dz\frac{dV}{dz}\,\frac{dn(M,z)}{dM}\,|\tilde{y}_l(M,z)|^2}{\int dz\frac{dV}{dz}\int dM\,\frac{dn(M,z)}{dM}\,|\tilde{y}_l(M,z)|^2}. \quad (26)$$

We find that massive haloes between $10^{14}\ h^{-1}\ M_\odot$ and $10^{15}\ h^{-1}\ M_\odot$ dominate C_l at $l = 3000$ with a peak at $3 \times 10^{14}\ h^{-1}\ M_\odot$. For $l = 1000$ the peak is at $5 \times 10^{14}\ h^{-1}\ M_\odot$, while for $l = 10000$ at $10^{14}\ h^{-1}\ M_\odot$. The large-angular-scale C_l is thus sensitive to the presence of very massive and rare haloes, which explains why the sampling variance is so large on large scales. Much smaller angular scales ($< 1'$ or $l > 10000$) receive significant contribution from smaller mass halos, where uncertain

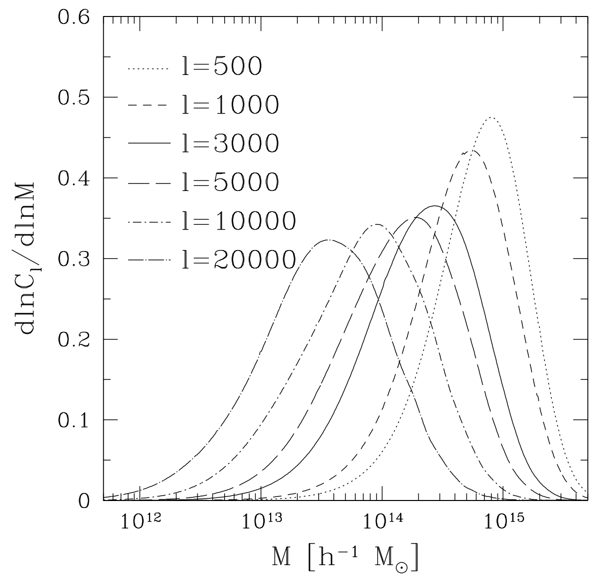

Figure 6. Mass distribution of C_l. We plot $d\ln C_l/d\ln M$, equation (26), for a given l. From right to left it is shown $l = 500$, 1000, 3000, 5000, 10000, and 20000, as indicated in the figure.

physics of gas cooling, heating, or star formation makes predictions unreliable; however, for the angular scales of $2' - 4'$ the dominant contribution is from massive ($10^{14} - 10^{15}\ h^{-1}\ M_\odot$) clusters for which these uncertainties are small and which are still so abundant that the sampling variance is small. Fortunately, this is precisely the range targeted by the next generation CMB experiments.

5 COVARIANCE MATRIX OF THE SZ ANGULAR POWER SPECTRUM

To determine the cosmological parameters from the power spectrum we need to know its covariance matrix. If fluctuations are Gaussian, then we can calculate the variance from the spectrum itself. If fluctuations are non-Gaussian, then the covariance matrix is no longer diagonal. In this case we need to know not only C_l, but also specific configurations of the angular trispectrum, the harmonic transform of the four-point correlation function, to estimate the covariance matrix.

We have already commented above that the SZ fluctuations observed in the hydrodynamic simulations are very non-Gaussian: the scatter among the C_l estimates is large, especially on large scales, and the estimates are strongly correlated. We must thus calculate the full covariance matrix, taking into account the non-Gaussianity. Here we will use both the halo approach (Cooray 2001), and the hydrodynamic simulations (Seljak, Burwell, & Pen 2001), to develop a reliable method for covariance matrix calculation.

The covariance matrix of C_l, $M_{ll'}$, is given by (Cooray 2001)

$$M_{ll'} \equiv \left\langle \left(C_l^{\rm obs} - C_l\right)\left(C_{l'}^{\rm obs} - C_{l'}\right)\right\rangle = f_{\rm sky}^{-1}\left[\frac{2\,(C_l)^2}{2l+1}\delta_{ll'} + \frac{T_{ll'}}{4\pi}\right], \quad (27)$$

where the angular bracket denotes the ensemble average, $f_{\rm sky}$ is a fraction of the sky covered by an experiment ($f_{\rm sky} = 1$ for all sky), $C_l^{\rm obs}$ the observationally measured power spectrum, and C_l the theoretically predicted power spectrum (equation 1). Note that $\left\langle C_l^{\rm obs}\right\rangle = C_l$. The second term in the r.h.s. represents the trispectrum contribution.

5.1 Halo approach to the angular trispectrum

In this section we calculate $M_{ll'}$, equation (27), using the halo approach, and compare it with the hydrodynamic simulations. An angular-trispectrum configuration is represented by a quadrilateral, and is characterized by four sides and one diagonal (Hu 2001). Among the trispectrum configurations, those which constitute two lines whose lengths are l and l', respectively, and have zero diagonal, determine the power-spectrum covariance matrix. We denote these as $T_{ll'}$ (equation 27).

Using the halo approach one obtains for the Poisson term which dominates the trispectrum (Cooray 2001),

$$T_{ll'} = g_\nu^4 \int_0^{z_{\max}} dz \frac{dV}{dz} \int_{M_{\min}}^{M_{\max}} dM \frac{dn(M,z)}{dM} \times \left|\tilde{y}_l(M,z)\right|^2 \left|\tilde{y}_{l'}(M,z)\right|^2, \quad (28)$$

where all the quantities have the same meaning as in equation (1). It follows from equation (27) that $(4\pi f_{\rm sky})^{-1}T_{ll'}$ determines the non-diagonal terms of $M_{ll'}$. Figure 7 shows $T_{ll'}$ divided by $C_lC_{l'}$. To make it represent a ratio of the "non-Gaussian error" (the second term in $M_{ll'}$ of equation 27) to the "Gaussian error" (the first term) we have plotted $T_{ll'}/(C_lC_{l'})$ multiplied by $\sqrt{(2l+1)(2l'+1)}/8\pi$, which is this ratio when $l = l'$. We find that the ratio decreases with l as $l^{-0.95}$, or equivalently, $T_{ll} \propto l^{-1.95}(C_l)^2$, for $l \gtrsim 10^3$.

Figure 7 also shows how $M_{ll'}$ scales with l for a given l'. In the limit of $T_{ll} \ll (C_l)^2$, the plotted quantity in figure 7 reduces to the correlation coefficient of C_l, $r_{ll'}$, given by

$$r_{ll'} \equiv \frac{M_{ll'}}{\sqrt{M_{ll}M_{l'l'}}} \approx \frac{\sqrt{(2l+1)(2l'+1)}}{8\pi}\frac{T_{ll'}}{C_lC_{l'}} \qquad \left(T_{ll} \ll C_l^2\right). \quad (29)$$

As $T_{ll'}/(C_lC_{l'})$ varies slowly with l for a given l', C_l and $C_{l'}$ remain highly correlated even for a large value of $|l - l'|$ (Cooray 2001). Because of this reason binning does not reduce the error bars as much as it would for Gaussian fluctuations.

5.2 Comparison with the simulated error bars

To compare the predicted error bars of C_l with the simulated ones one must take into account binning or band averaging that the simulations use to produce C_l. If the binned C_l at a given l is the average of C_l between $l - \Delta l/2 \le l \le l + \Delta l/2$, then the covariance matrix is

$$M_{ll'} \approx f_{\rm sky}^{-1}\left[\frac{2\,(C_l)^2}{(2l+1)\Delta l}\delta_{ll'} + \frac{T_{ll'}}{4\pi}\right]. \quad (30)$$

Here, we have assumed that $\Delta l \ll l$. Since both C_l and $T_{ll'}$ are sufficiently smooth, the binning does not affect the values of C_l and $T_{ll'}$ as long as $\Delta l \ll l$. We find that $\Delta l/l < 0.1$ suffices for this approximation to hold.

Figure 8 compares the predicted fractional errors of C_l, $\Delta C_l/C_l \equiv \sqrt{M_{ll}}/C_l$, with the simulated ones. We find that the

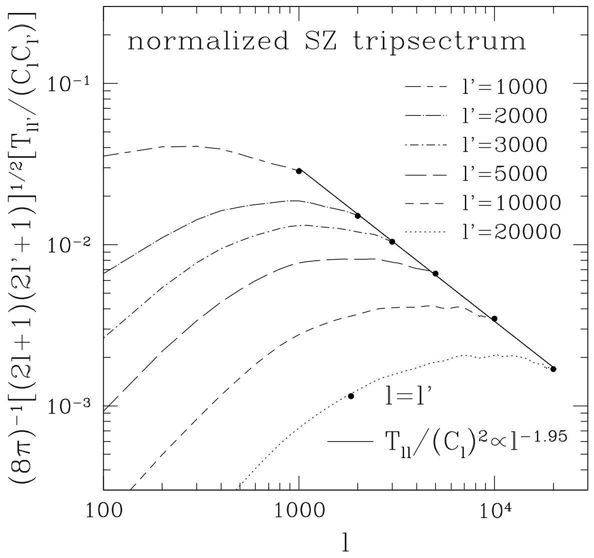

Figure 7. The SZ angular trispectrum, $T_{ll'}$, multiplied by $\sqrt{(2l+1)(2l'+1)}/C_lC_{l'}$. From top to bottom it is shown $l' = 1000$, 2000, 3000, 5000, 10000, and 20000, as indicated in the figure. The solid line shows $\propto l^{-0.95}$, which means that the ratio of the non-Gaussian error to the Gaussian error decreases with l as $l^{-0.95}$, and T_{ll} scales as $\propto l^{-1.95}(C_l)^2$. The plotted quantity reduces to the correlation coefficient of C_l in the limit of $T_{ll} \ll (C_l)^2$.

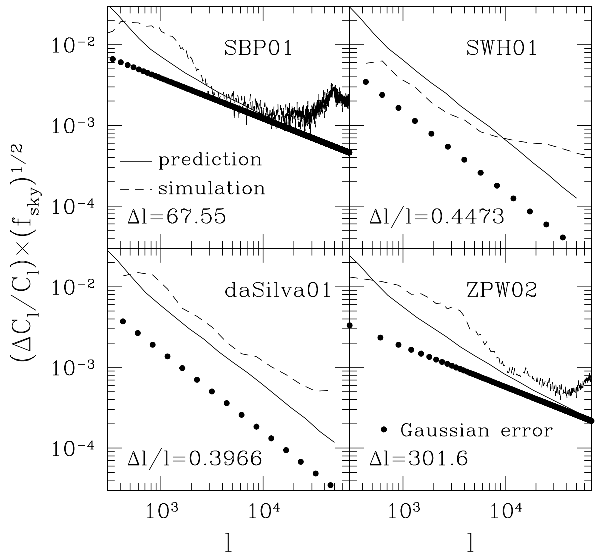

Figure 8. Predicted fractional r.m.s. errors of C_l, $\Delta C_l/C_l \equiv \sqrt{M_{ll}}/C_l$, in comparison with the simulated errors (see table 1 for the meaning of the labels shown in each panel, and for the cosmological parameters used). We have multiplied the simulated errors by the square-root of a fraction of the sky covered by the simulations, $f_{\rm sky}$. The solid lines show the predicted fractional errors, while the dashed lines show the simulated ones. The filled circles show Gaussian approximation to the fractional errors, $\simeq (l\Delta l)^{-1/2}$ for $l \gg 1$, where Δl is the binning size shown in each panel. The predicted errors agree with the simulated ones within a factor of two, providing a significant improvement over the Gaussian approximation.

predictions agree with the simulations within a factor of two, similar to the agreement we have found for the spectrum itself. There is no clear trend in the residuals and we both ovepredict and underpredict the variance compared to the simulations. Since the variance is very sensitive to the sampling errors, it is possible that some of the discrepancy is caused by insufficient sampling in the simulations. Figure 8 also plots Gaussian approximation to the errors, showing that our predictions give a significant improvement over the Gaussian approximation. We have also compared the predicted correlation coefficient, $r_{ll'}$ (equation 29), with the simulations of Seljak et al. (2001), finding a good agreement between the two and confirming that for high l the neighboring bins in C_l are strongly correlated if the binning is sufficiently broad for the trispectrum term to dominate. Proper modeling of cross-correlations between the bins is essential for the parameter-error estimation and for the proper treatment of the statistical significance of results.

6 DETERMINATION OF POWER-SPECTRUM AMPLITUDE

In this section, we analyze how well we can determine σ_8 by measuring the SZ angular power spectrum with realistic observations, and apply it to the recent CBI results (Mason et al. 2002).

We perform a least-square fitting to C_l by calculating χ^2,

$$\chi^2 \equiv \sum_{l\leq l'} \left(\hat{C}_l - C_l\right) \left(M^{-1}\right)_{ll'} \left(\hat{C}_{l'} - C_{l'}\right), \tag{31}$$

where $\hat{C}_l$ is a reference power spectrum which uses the fiducial cosmological parameters, or the actual CBI data. We determine the confidence levels of the parameter estimation by calculating $\Delta\chi^2$.

We vary $\Omega_{\rm m}$ and σ_8, i.e., $\chi^2 = \chi^2(\Omega_{\rm m}, \sigma_8)$. We fix the other parameters at the fiducial values, $\Omega_\Lambda = 1 - \Omega_{\rm m}$, $\Omega_{\rm b} = 0.05$, $h = 0.7$, $w = -1.0$, and $n = 1.0$. For a given set of cosmological parameters, we calculate C_l and $M_{ll'}$ and then obtain χ^2. By approximating probability distribution function of C_l with a Gaussian we have $\Delta\chi^2 = 2.30, 6.17$, and 11.8 for 68.3%, 95.4%, and 99.7% confidence levels (C.L.), respectively.

First, we assume that experiments are sampling-variance limited for $2000 < l < 3000$, or $2000 < l < 5000$; thus, we consider a few arcminutes angular resolution and ignore instrumental noise. To save computational time we do not evaluate equation (31) at every l, but at 10 points for $2000 < l < 3000$, or 20 points for $2000 < l < 5000$. This choice gives $\Delta l = 111$ and 158, respectively, in equation (30). Both C_l and $T_{ll'}$ are smooth so that this is a good approximation.

For the sky coverage we consider 1 deg^2 or 10 deg^2 survey of the sky. These parameters are characteristic for the on-going or forthcoming experiments: CBI (Padin et al. 2001) for $2000 < l < 3000$ and 1 deg^2, SZA (Holder & Carlstrom 2001) for $2000 < l < 3000$ and 10 deg^2, AMIBA (Zhang, Pen, & Wang 2002) or ACT (Lyman Page, private communication) for $2000 < l < 5000$ and 10 deg^2. AMIBA and ACT experiments are actually going to survey about 100 deg^2 of the sky, so that the actual constraints to be obtained from these experiments would be better than we show here.

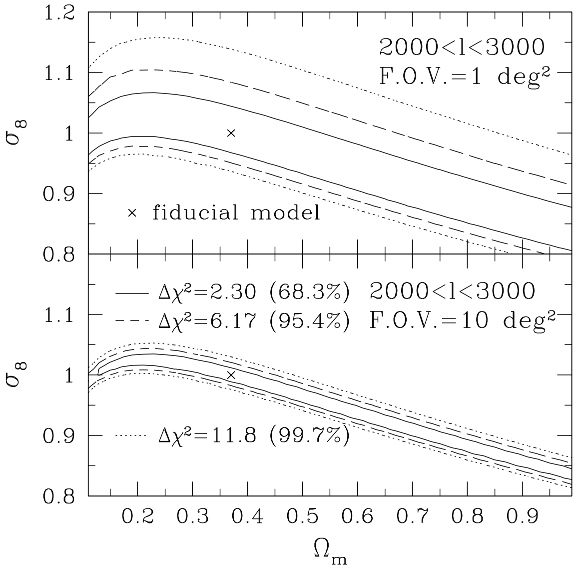

Figure 9. Contours showing how well we can determine σ_8 against $\Omega_{\rm m}$ by measuring the SZ angular power spectrum with realistic observations. We consider those observations which measure C_l between $2000 < l < 3000$, and survey 1 deg^2 (top panel), or 10 deg^2 (bottom panel) of the sky. The top panel is similar to the CBI experiment and the bottom panel to the SZA experiment. The solid line shows $\Delta\chi^2 = 2.30$ (68.3% C.L.), the dashed line $\Delta\chi^2 = 6.17$ (95.4% C.L.), and the dotted line $\Delta\chi^2 = 11.8$ (99.7% C.L.). The cross marks the fiducial cosmological model. We find that the contour is very sensitive to σ_8, yet almost independent of $\Omega_{\rm m}$ at around $\Omega_{\rm m} \sim 0.2$ (see also section 4). We find that a CBI-type observation should be able to determine σ_8 to within 10% at 2σ, while a SZA-type to within 5% at the same level.

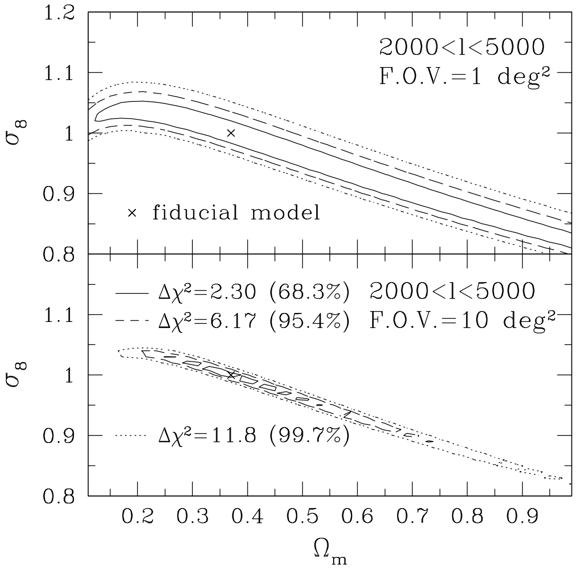

Figure 10. The same figure as figure 9, but for $2000 < l < 5000$. We find that statistical errors on σ_8 are very small for a 10 deg^2 survey, showing that ACT or AMIBA experiments which survey about 100 deg^2 of the sky determine σ_8 with theoretical-uncertainty-limited accuracy ($\sim$ 10%). A 1 deg^2 survey shown in the top panel is sufficient enough to determine σ_8 with that accuracy.

Figure 9 shows χ^2 on a $\Omega_{\rm m} - \sigma_8$ plane for the $2000 < l < 3000$ region. The solid line shows $\Delta\chi^2 = 2.30$ (68.3% C.L.), the dashed line $\Delta\chi^2 = 6.17$ (95.4% C.L.), and the dotted line $\Delta\chi^2 = 11.8$ (99.7% C.L.). The top panel uses 1 deg^2 of the sky, close to the CBI experiment (if it is sampling-variance limited), while the bottom panel uses 10 deg^2 of the sky, close to the SZA experiment. We find that the contours are very sensitive to σ_8 and almost independent of $\Omega_{\rm m}$ for $0.15 < \Omega_{\rm m} < 0.4$ (Komatsu & Kitayama 1999). This is consistent with what we have previously shown in section 4 (see equation 23). While for one degree sky coverage the sampling-variance error is similar to the systematic (theoretical) error (10% at the 95% confidence level), a 10-times larger survey like SZA with the same angular resolution should be able to determine σ_8 to within 5% at the same level, so at that point the errors will be dominated by the theoretical uncertainty rather than by statistics.

Figure 10 shows constraints on a $\Omega_{\rm m} - \sigma_8$ plane which would be obtained with ACT or AMIBA, whose angular resolution is $1' - 2'$. The figure uses $2000 < l < 5000$ with 1 deg^2 (top panel) or 10 deg^2 (bottom panel) sky coverage. We find that the statistical error on σ_8 is extremely small for a 10 deg^2 survey. Surveys such as ACT or AMIBA covering about 100 deg^2 of the sky will determine σ_8 with accuracy limited by the theoretical uncertainty. This is currently at a $\sim 10\%$ level and obviously more theoretical work should improve it in order for the power of the upcoming CMB experiments to be maximally exploited. It is of course still useful to cover such a large area of the sky, since this will allow us to use a bootstrap error determination without relying on the simulations.

Recently, CBI team announced a detection of CMB power up to $l \sim 3000$, which at a face value is inconsistent with the primary CMB alone (Mason et al. 2002). Figure 11 compares the CBI data (Mason et al. 2002) (light-gray shaded area, which assumes Gaussian errors) to the predicted SZ angular power spectra for $\sigma_8 = 0.95$, 1.05, and 1.15 (thin solid lines). We also show the primary CMB anisotropy for the fiducial cosmological model (dashed line), and the sum of the two for $\sigma_8 = 1.05$ (thick solid line). The predicted non-Gaussian errors are shown for $\sigma_8 = 1.05$ (dark-gray shaded area). We have included the instrumental-noise power spectrum in the non-Gaussian errors by using the noise power spectrum shown in figure 4 of Mason et al. (2002), and assuming the sky coverage of 1 deg^2. From the figure one can see that the CBI data favor $\sigma_8 \sim 1$ models, and the predicted power spectra can explain the detected excess power reasonably well.

We fitted the data to the predicted SZ angular power spectrum using the four bins shown in figure 11 and computing χ^2 from equation (31). We compute the covariance matrix using equation (30) with the bin-size of $\Delta l = (565, 378, 612, 1000)$ for each bin. For example, we have obtained $(327, 394, 364, 425)\mu\,{\rm K}^2$ for $\sigma_8 = 1.05$. The cross-correlation between the bins is most significant for the first bin, for which the correlation coefficients with the other 3 bins are $(0.46, 0.41, 0.29)$. The remaining 3 coefficients are below 0.3. Figure 12 shows confidence-level contours on the $\Omega_{\rm m} - \sigma_8$ plane for the CBI data. The top panel (a) assumes that the detection of the excess power in the four bins is entirely due to the SZ effect (i.e., we ignore the primary CMB anisotropy). We find $\sigma_8(\Omega_{\rm b}h/0.035)^{2/7} = 1.05 \pm 0.15$ at 95% confidence limit for $0.1 < \Omega_{\rm m} < 0.5$.

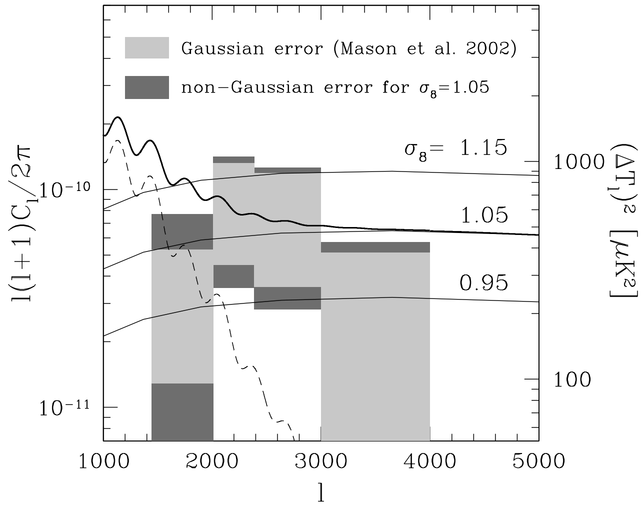

Figure 11. The CBI data (Mason et al. 2002) with Gaussian errors (light-gray shaded area), the predicted SZ angular power spectra for $\sigma_8 = 0.95$, 1.05, and 1.15 (thin solid lines), the primary CMB anisotropy for the fiducial cosmological model (dashed line), and the sum of the two for $\sigma_8 = 1.05$ (thick solid line). The dark-shaded area gives non-Gaussian errors predicted for $\sigma_8 = 1.05$.

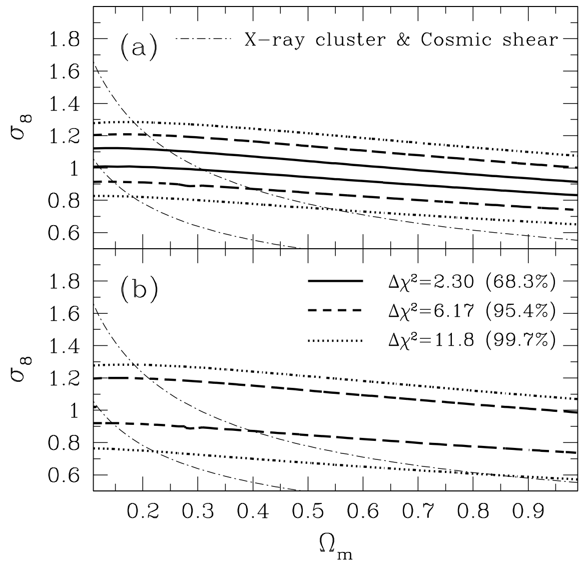

Figure 12. The CBI constraint on the $\Omega_{\rm m} - \sigma_8$ plane. The top panel (a) assumes that the CBI data shown in figure 11 are entirely due to the SZ effect. The meaning of the contour lines is the same as in figure 9. The cluster abundance and cosmic-shear constraints are shown in the figure as $\sigma_8\Omega_{\rm m}^{0.5} = 0.45 \pm 0.1$, which roughly summarizes the current uncertainty from these methods. The bottom panel (b) assumes that the first bin of the CBI data is affected by the primary CMB anisotropy. In both cases, we find $\sigma_8(\Omega_{\rm b}h/0.035)^{2/7} = 1.05 \pm 0.15$ at the 95.4% confidence level for $0.1 < \Omega_{\rm m} < 0.5$.

The cluster abundance and cosmic-shear constraints are also shown in the figure as $\sigma_8\Omega_{\rm m}^{0.5} = 0.45 \pm 0.1$, which roughly summarizes the current (systematic dominated) uncertainty from these methods. Combining the two can break the degeneracy between σ_8 and $\Omega_{\rm m}$ and is leading to $\sigma_8 \sim 1$, $\Omega_{\rm m} \sim 0.2$. One should be cautious not to overinterpret this conclusion, since systematic effects in both are still very large and could affect the parameter determination.

The bottom panel (b) assumes that the $l \sim 1700$ bin is affected by the primary CMB anisotropy, while the other bins are entirely due to the SZ effect. We assume that the primary CMB is 400 μK^2 at the first bin, roughly consistent with the best-fitting theoretical curve, and is negligible in the other three bins. In principle we should change the primary CMB as well as we change the cosmological parameters; however, for simplicity we just use 400 μK^2 regardless of the cosmological parameters. We find the same constraint on the $\Omega_{\rm m} - \sigma_8$ plane as in the panel (a), i.e., $\sigma_8(\Omega_{\rm b}h/0.035)^{2/7} = 1.05 \pm 0.15$ at the 95% confidence limit for $0.1 < \Omega_{\rm m} < 0.5$. We however find that models with $\Omega_{\rm m} > 0.1$ are excluded at the 68% confidence limit. This may indicate that the first bin of the CBI data is too low for the SZ interpretation on small angular scales. Decreasing $\Omega_{\rm m}$ to very low values increases the errors of C_l at lower l, so the statistical weight of the lowest-l bin decreases making χ^2 more favorable. But the statistical significance of this is very low and the uncertainties in the covariance matrix are still sufficiently large that one should not overinterpret the results. At $\Omega_{\rm m} = 0.2$ we find $\chi^2 = 3.4$ in this case (b) as opposed to 2.3 in the case (a)above; thus, both have acceptable goodness-of-fit for 3 degrees of freedom. In general, the CBI data are consistent with detection of the SZ fluctuations, and imply $\sigma_8(\Omega_{\rm b}h/0.035)^{2/7} = 1.05 \pm 0.15$, but a somewhat larger survey is needed to confirm this interpretation. The good news is that with a survey just a few times the survey area of CBI one should be able to determine σ_8 with an accuracy comparable to or better than any other current observations and with a different, and perhaps smaller, systematic uncertainty.

7 UNCERTAINTIES IN THE PREDICTIONS

The predictions are very sensitive to the halo mass function, so we investigate how the prediction changes if using different formulae in the literature. We compare four different predictions for C_l computed with four different formulae for the mass function: (JB3) Jenkins et al.'s τCDM mass function that uses the SO mass with $\delta = 180\Omega_{\rm m}(z)$ (Jenkins et al. 2001), (J9) Jenkins et al.'s universal mass function that uses the FOF mass (equation 9 of Jenkins et al. 2001) and includes smoothing which may systematically increase the mass function in the exponential tail (Hu & Kravtsov 2002), (HV) Evrard et al.'s Hubble-volume mass function which uses the SO mass with $\delta = 200$ (Evrard et al. 2001), and (PS) Press & Schechter's mass function which uses the virial mass (Press & Schechter 1974) (this one is of interest just for historical comparison). As Jenkins et al. (2001) note that the FOF mass they use corresponds to the SO mass with $\delta = 180\Omega_{\rm m}(z)$, we use the SO mass to calculate the mass function of (J9).

The top-left panel (a) of figure 13 compares C_l computed with the four different mass functions. We find a very good agreement between (JB3) and (HV), while (J9) predicts higher amplitude. Hu & Kravtsov (2002) have also found that the mass function of (J9)

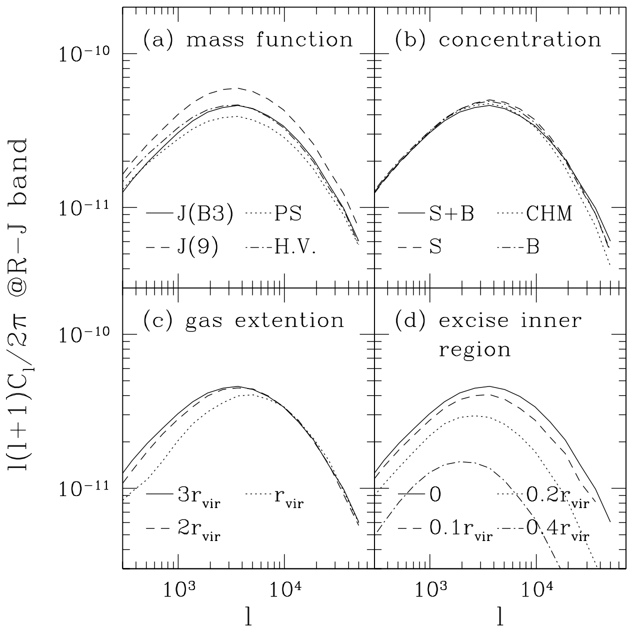

Figure 13. Theoretical uncertainty in the SZ angular power spectrum. (**a**) Uncertainty in the dark-matter-halo mass function. The solid line shows the prediction with Jenkins et al.'s τCDM mass function (equation 6), the dashed line Jenkins et al.'s universal mass function (equation 9 of Jenkins et al. (2001)), and the dot-dashed line Evrard et al.'s Hubble-volume mass function (Evrard et al. 2001). For comparison, the dotted line plots the prediction with Press & Schechter's mass function (Press & Schechter 1974). (**b**) Uncertainty in the concentration parameter. (**c**) Uncertainty in the hot-gas extension in haloes. The solid line shows C_l with the hot-gas extension cut out at 3 times the virial radius, the dashed line at 2 times the virial radius, and the dotted line at the virial radius. (**d**) Uncertainty in the inner gas-pressure profile. The solid line shows C_l with no excision, the dashed line shows the one with the region interior to 10% of the virial radius excised, the dotted line 20% of the virial radius, and the dot-dashed line 40% of the virial radius. The dominant contribution to the spectrum is from $20\% - 40\%$ of the virial radius

predicts too many high-mass haloes to agree with their N-body simulations, and concluded that the smoothing used for deriving (J9) causes the high-mass halo abundance to increase anomalously. Jenkins et al. (2001) have explained this in their paper: when deriving (J9), they are mainly interested in small-mass haloes for which the smoothing is less significant. Press & Schechter's mass function predicts lower amplitude and underestimates the abundance of high-mass haloes compared with N-body simulations (Jenkins et al. 2001). As the SZ effect is dominated by the high-mass haloes, we should not use (J9) and (PS), but (JB3) or (HV).

Since there is no single expression for the concentration parameter c (see equation 10 for definition) we need to quantify how much uncertainty in C_l is due to the uncertainty in the concentration parameter. To quantify this, we use four different formulae for the concentration parameter: (S+B) power-spectrum-determined concentration parameter at $z = 0$ (Seljak 2000) but evolved by $(1 + z)^{-1}$, for which evolution has been measured in N-body simulations (Bullock et al. 2001), (S) power-spectrum determination with the non-linear mass evaluated at z, (B) halo determination of the concentration parameter (Bullock et al. 2001) and (CHM) a different power-spectrum-determined concentration parameter (Cooray, Hu, & Miralda-Escudé 2000). The top-right panel (b) of figure 13 shows the predictions computed with the four different concentration parameters. We find that the uncertainty in the concentration parameter has little effect on C_l.

How sensitive are the results to the outer radius of the gas profile (shock radius), where the gas temperature rapidly drops to IGM values? Previous work on a gas profile has assumed that the hot gas in haloes extends only up to the virial radius, but numerical simulations suggest a smooth decrease in temperature at least out to twice the virial radius (Bryan & Norman 1998; Eke, Navarro, & Frenk 1998; Frenk et al. 1999). The bottom-left panel (c) of figure 13 shows the predicted C_l with the hot-gas extension cut out at 1, 2, or 3 times the virial radius. While a cut-off at the virial radius suppresses C_l at $l < 5000$, there is little difference for the cut-off at $2r_{\rm vir}$ and beyond. One should thus include the hot-gas extension beyond the virial radius; otherwise, one underestimates the power spectrum on large angular scales, but the actual position of the cut-off is not very important since the power spectrum converges at $2r_{\rm vir}$.

The gas density profile in the inner region displays a core (Bryan & Norman 1998; Eke, Navarro, & Frenk 1998; Frenk et al. 1999), which is well reproduced by our model (Komatsu & Seljak 2001). On the other hand, recent X-ray observations have observed a decrease in temperature toward the centre within 5% of the virial radius (McNamara et al. 2000; Allen, Ettori, & Fabian 2001; Allen et al. 2001; Arnaud et al. 2001a; Arnaud et al. 2001b; Kaastra et al. 2001), which our polytropic model does not account for. The bottom-right panel (d) of figure 13 shows the predicted C_l with the inner region within 10%, 20%, or 40% of the virial radius excised. We find that the region interior to 10% of the virial radius has a negligible contribution to C_l, so the pressure profile in the cluster core has no effect on C_l. From this figure we find that the dominant contribution to C_l comes from around $20\% - 40\%$ of the virial radius, roughly corresponding to r_{2500}, which is just in the range of *Chandra* satellite for medium redshift clusters (McNamara et al. 2000; Allen, Ettori, & Fabian 2001; Allen et al. 2001) and well within *XMM/Newton* or *BeppoSax* (Arnaud et al. 2001a; Arnaud et al. 2001b; Kaastra et al. 2001). Recent observations confirm that the gas profile agrees well with the dark-matter profile in this region (Allen, Schmidt, & Fabian 2002), confirming our basic assumption. We note that the temperature gradient is still small over this range, so most of the pressure gradient is caused by the gas-density profile.

The effect of non-adiabatic physics has been investigated with hydrodynamic simulations. In da Silva et al. (2001b) it has been claimed that radiative cooling reduces C_l by modest amount, $20\% - 40\%$, on all angular scales. This is presumably due to a decrease in the gas fraction, since some fraction of gas is being transformed into stars. Despite their extreme cooling treatment (giving too much cooled material to match the observations) the effect of radiative cooling is modest (note that 40% change in C_l gives a 5% change in σ_8). Preheating may lead to a larger effect, as it may alter the gas structure not only in the inner region, but also at larger radii, especially for smaller-mass haloes. Some fraction of the gas may be expelled from the cluster, which would suppress the SZ fluctuations on small scales. At the same time, preheating increases the gas temperature, which would increase the spectrum. However, care must be taken not to violate the FIRAS constraints on the mean y parameter and it is unlikely that this could significantly enhance the SZ power spectrum without violating these limits. Several authors have noticed significant effects of preheating on C_l (Springel, White, & Hernquist 2001; Holder & Carlstrom 2001; da Silva et al. 2001b), although current treatments are still over-simplified. One must be careful in analytic models to make them self-consistent, as one cannot retain gas in hydrostatic equilibrium within external dark-matter potential using a large gas core and isothermal gas. When hydrostatic equilibrium is imposed the pressure profile is less affected than the density or temperature profiles. It is likely that any preheating will have only a modest effect on the SZ power spectrum.

8 CONCLUSIONS

In this paper we present a refined analytic model for the angular power spectrum of the SZ effect. In contrast to previous modeling (Atrio-Barandela & Mücket 1999; Komatsu & Kitayama 1999; Cooray 2000; Molnar & Birkinshaw 2000; Holder & Carlstrom 2001; Zhang & Pen 2001), our model has no free parameters and treats the gas in a cluster dark-matter potential self-consistently, using the universal gas-density and temperature profile (Komatsu & Seljak 2001), which fits the observed and the simulated properties of clusters of galaxies in the range of interest to the SZ observations (outside 5% of the virial radius).

We compare our predictions for the spectrum and the errors with the hydrodynamic SZ simulations and find a good agreement. The deviations between our model and the simulations are comparable to the deviations among the simulations themselves and are particularly small in the observationally relevant range around $l \sim 3000$. Some of the discrepancies are due to either poor resolution in the simulations or sampling variance, while the remaining difference could be due to the simplifying assumptions of gas physics in our model, such as hydrostatic equilibrium, spherical symmetry, merging and substructure, which may be inaccurate in particular at higher redshifts when the clusters are still forming. The disagreement is more important on very small angular scales ($l > 5000$), while the accuracy of our predictions in the range of $l \sim 2000 - 5000$ is better than a factor of two, which translates to less than 10% systematic uncertainty in the amplitude of fluctuations σ_8. We also compare analytic predictions for the power-spectrum covariance matrix to the simulations and find similarly good agreement.

We investigate the dependence of C_l on various cosmological parameters, finding that over the range of interest σ_8 and $\Omega_b h$ determine the amplitude of C_l almost entirely, as has been pointed out by several authors before as well (Komatsu & Kitayama 1999; Seljak et al. 2001; Zhang & Pen 2001; Zhang et al. 2002). It is particularly important that the matter density of the universe does not affect the spectrum as much as σ_8 does, in agreement with Komatsu & Kitayama (1999). This differs from the local-cluster-abundance studies, where the constraint is usually on $\sigma_8\Omega_m^{0.5}$.

The dominant contribution to C_l comes from massive clusters ($M > 10^{14}\ h^{-1}\ M_\odot$ for $l < 5000$) at moderate ($z \sim 1$) redshift. Within the cluster, the dominant contribution comes from around $0.2 - 0.4 r_{\rm vir}$, suggesting that the physical processes taking place in the cluster core such as cooling, heating or heat conduction have little effect on the SZ power spectrum. We assume that the gas fraction is close to the cosmic mean baryon fraction, which is reasonable for massive clusters and has observational support in low stellar-mass-to-cluster-mass ratios in massive clusters (e.g., Fukugita, Hogan, & Peebles 1998), as well as in studies of the gas fraction as a function of radius (e.g., Allen, Schmidt, & Fabian 2002). While more exotic mechanisms such as preheating could affect C_l on all scales (by increasing the temperature and/or reducing the gas clumping), they are constrained by the FIRAS limits and are unlikely to make more than a factor of two change in C_l (comparable to a 10% change in σ_8).

Using analytic predictions for the spectrum and its covariance matrix we have performed a likelihood analysis to estimate how well we can measure σ_8 against Ω_m with realistic SZ observations. The likelihood is very sensitive to σ_8 almost independent of Ω_m (figure 9 or 10). By performing the likelihood analysis on the recently reported CBI detection (Mason et al. 2002) at the level of 20 μK ($l(l+1)C_l/(2\pi) \simeq 5.4\times10^{-11}$) at around $l \sim 2000-3000$ (figure 11), we find $\sigma_8(\Omega_b h/0.035)^{2/7} = 1.05 \pm 0.15$ at the 95% statistical confidence level. To this we should add about 10% systematic theoretical uncertainty due to the simplified modeling in our model, the numerical issues in the simulations, and missing physics in both. We should note that most of the effects we have ignored within our model tend to further increase σ_8: assumed fiducial value for $\Omega_b h = 0.035$ is somewhat high, we ignored fraction of gas transformed into stars, and our predictions are somewhat higher than the simulation results at $2000 < l < 3000$ relevant for CBI. These effects would further increase σ_8, although not by more than $5\% - 10\%$. Such a high value for σ_8 is in tension with the primary CMB amplitude determination (Lahav et al. 2001) and Ly-α forest determination (Croft et al. 1999; McDonald et al. 2000), although it can be accommodated by the cluster abundance and the weak lensing results if $\Omega_m \sim 0.2 \pm 0.1$. While the CBI experiment is surveying 1 deg^2 of the sky and still has a large instrumental noise, a somewhat larger sky coverage with lower noise (e.g., SZA) would significantly reduce the statistical errors on σ_8. Surveys with 100 deg^2 such as ACT or AMIBA should be able to measure both the power spectrum and its covariance matrix (e.g. by using bootstrap sampling) to exquisite precision.

In conclusion, measurement of the angular power spectrum of the SZ effect offers a promising way to determine σ_8, since it is very sensitive to its value and is almost independent of Ω_m. It is free of observational selection effects such as flux, surface brightness, or volume limit of the survey. It does not require the mass of sampled haloes to be measured, and there is no uncertainty associated with the mass–flux calibration. Finally, it is within reach of the next generation of small-scale CMB experiments and may have already been detected by the CBI experiment, in which case their results imply that the amplitude of fluctuations at 8 h^{-1} Mpc scale is of order unity.

ACKNOWLEDGMENTS

We would like to thank Antonio C. da Silva, Alexandre Refregier, Volker Springel, Pengjie Zhang, and their collaborators for providing us with their hydrodynamic simulation data results. We would like to thank John E. Carlstrom, Carlo Contaldi, Gilbert P. Holder, Wayne Hu, Andrey V. Kravtsov, Ue-Li Pen, Masahiro Takada, and Pengjie Zhang for discussions. U. S. acknowledges the support of NASA and Packard and Sloan Foundation Fellowships.

REFERENCES

Allen S. W., Ettori S., Fabian A. C., 2001, MNRAS, 324, 877
Allen S. W., Schmidt R. W., Fabian A. C., 2001, MNRAS, 328, L37
Allen S. W., Schmidt R. W., Fabian A. C., 2002, MNRAS, in press (astro-ph/0205007)
Allen S. W. et al., 2001, MNRAS, 324, 842
Arnaud M. et al., 2001a, A&A, 365, L67

Arnaud M., Neumann D. M., Aghanim N., Gastaud R., Majerowicz S., Hughes J. P., 2001b, A&A, 365, L80
Atrio-Barandela F., Mücket J. P., 1999, ApJ, 515, 465
Bahcall N. A., Fan X., 1998, ApJ, 504, 1
Bardeen J. M., Bond J. R., Kaiser N., Szalay A. S., 1986, ApJ, 304, 15
Bean R., Melchiorri A., 2002, Phys. Rev. D, 65, 41302
Birkinshaw M., 1999, Phys. Rep., 310, 97
Bond J. R. et al., 2002, ApJ, submitted (astro-ph/0205386)
Bryan G. L., Norman M. L., 1998, ApJ, 495, 80
Bullock J. S., Kolatt T. S., Sigad Y., Somerville R. S., Kravtsov A. V., Klypin A. A., Primack J. R., Dekel A., 2001, MNRAS, 321, 559
Church S. E., Ganga K. M., Ade P. A. R., Holzapfel W. L., Mauskopf P. D., Wilbanks T. M., Lange A. E., 1997, ApJ, 484, 523
Cole S., Kaiser N., 1988, MNRAS, 233, 637
Cooray A., 2000, Phys. Rev. D, 62, 103506
Cooray A., 2001, Phys. Rev. D, 64, 63514
Cooray A., Hu W., Miralda-Escudé J., 2000, ApJ, 535, L9
Croft R. A. C., Weinberg D. H., Pettini M., Hernquist L., Katz N., 1999, ApJ, 520, 1
da Silva A. C., Barbosa D., Liddle A. R., Thomas P. A., 2000, MNRAS, 317, 37
da Silva A. C., Barbosa D., Liddle A. R., Thomas P. A., 2001a, MNRAS, 326, 155
da Silva A. C., Kay S. T., Liddle A. R., Thomas P. A., Pearce F. R., Barbosa D., 2001b, ApJ, 561, L15
Dawson K. S., Holzapfel W. L., Carlstrom J. E., Joy M., LaRoque S. J., Reese E. D., 2001, ApJ, 553, L1
Eke V. R., Cole S., Frenk C. S., 1996, MNRAS, 282, 263
Eke V. R., Navarro J. F., Frenk C. S., 1998, ApJ, 503, 569
Eke V. R., Navarro J. F., Steinmetz M., 2001, ApJ, 554, 114
Evrard A. E. et al., 2001, ApJ, in press (astro-ph/0110246)
Frenk C. S. et al., 1999, ApJ, 525, 554
Fukugita M., Hogan C. J., Peebles P. J. E., 1998, ApJ, 503, 518
Ganga K., Ratra B., Church S. E., Sugiyama N., Ade P. A. R., Holzapfel W. L., Mauskopf P. D., Lange A. E., 1997, ApJ, 484, 517
Haiman Z. ., Mohr J. J., Holder G. P., 2001, ApJ, 553, 545
Holder G. P., Carlstrom J. E., 2001, ApJ, 558, 515
Holzapfel W. L., Carlstrom J. E., Grego L., Holder G., Joy M., Reese E. D., 2000, ApJ, 539, 57
Hu W., 2001, Phys. Rev. D, 64, 83005
Hu W., Kravtsov A. V., 2002, ApJ, submitted (astro-ph/0203169)
Jenkins A., Frenk C. S., White S. D. M., Colberg J. M., Cole S., Evrard A. E., Couchman H. M. P., Yoshida N., 2001, MNRAS, 321, 372
Jing Y. P., Suto Y., 2000, ApJ, 529, L69
Kaastra J. S., Ferrigno C., Tamura T., Paerels F. B. S., Peterson J. R., Mittaz J. P. D., 2001, A&A, 365, L99
Kitayama T., Suto Y., 1997, ApJ, 490, 557
Klypin A., Kravtsov A. V., Bullock J. S., Primack J. R., 2001, ApJ, 554, 903
Komatsu E., Kitayama T., 1999, ApJ, 526, L1
Komatsu E., Seljak U., 2001, MNRAS, 327, 1353
Lacey C., Cole S., 1993, MNRAS, 262, 627
Lahav O. et al., 2001, MNRAS, in press (astro-ph/0112162)
Makino N., Sasaki S., Suto Y., 1998, ApJ, 497, 555
Makino N., Suto Y., 1993, ApJ, 405, 1
Mason B. S. et al., 2002, ApJ, submitted (astro-ph/0205384)
McDonald P., Miralda-Escudé J., Rauch M., Sargent W. L. W., Barlow T. A., Cen R., Ostriker J. P., 2000, ApJ, 543, 1
McNamara B. R. et al., 2000, ApJ, 534, L135
Molnar S. M., Birkinshaw M., 2000, ApJ, 537, 542
Moore B., Governato F., Quinn T., Stadel J., Lake G., 1998, ApJ, 499, L5
Nakamura T. T., Suto Y., 1997, Progress of Theoretical Physics, 97, 49
Navarro J. F., Frenk C. S., White S. D. M., 1997, ApJ, 490, 493
Padin S. et al., 2001, ApJ, 549, L1
Partridge R. B., Richards E. A., Fomalont E. B., Kellermann K. I., Windhorst R. A., 1997, ApJ, 483, 38
Pearce F. R., Couchman H. M. P., 1997, New Astronomy, 2, 411
Pen U., 1998, ApJS, 115, 19
Persi F. M., Spergel D. N., Cen R., Ostriker J. P., 1995, ApJ, 442, 1
Pierpaoli E., Scott D., White M., 2001, MNRAS, 325, 77
Press W. H., Schechter P., 1974, ApJ, 187, 425
Refregier A., Komatsu E., Spergel D. N., Pen U., 2000, Phys. Rev. D, 61, 123001
Refregier A., Teyssier R., 2000, PRD, submitted (astro-ph/0111285)
Scaramella R., Cen R., Ostriker J. P., 1993, ApJ, 416, 399
Seljak U., 2000, MNRAS, 318, 203
Seljak U., 2001, MNRAS, submitted (astro-ph/0111362)
Seljak U., Burwell J., Pen U., 2001, Phys. Rev. D, 63, 619
Springel V., White M., Hernquist L., 2001, ApJ, 549, 681
Subrahmanyan R., Kesteven M. J., Ekers R. D., Sinclair M., Silk J., 1998, MNRAS, 298, 1189
Sugiyama N., 1995, ApJS, 100, 281
Sunyaev R. A., Zeldovich I. B., 1980, ARA&A, 18, 537
Teyssier R., 2002, A&A, 385, 337
Van Waerbeke L., Mellier Y., Pello R., Pen U.-L., McCracken H. J., Jain B., 2002, A&A, submitted (astro-ph/0202503)
Viana P. T. P., Liddle A. R., 1996, MNRAS, 281, 323
Viana P. T. P., Nichol R. C., Liddle A. R., 2002, ApJ, 569, L75
White M., 2001, A&A, 367, 27
White S. D. M., Efstathiou G., Frenk C. S., 1993, MNRAS, 262, 1023
Zhang P., Pen U., 2001, ApJ, 549, 18
Zhang P., Pen U., Wang B., 2002, ApJ, submitted (astro-ph/0201375)

Table 1. Simulation parameters. The first column assigns a label to each simulation. The second column shows the name of a code which each simulation uses: MMH (=Moving-Mesh Hydrodynamic code) (Pen 1998), and RAMSES (adaptive mesh-refinement hydrodynamic code) (Teyssier 2002) are mesh codes, while GADGET (=GAlaxies with Dark matter and Gas intEracT code) (Springel, White, & Hernquist 2001), and HYDRA (Pearce & Couchman 1997) are SPH (=Smoothed-Particle Hydrodynamic) codes. The third column shows the number of grids for mesh codes (MMH and RAMSES), or the number of SPH particles for SPH codes (GADGET and HYDRA). The box size of simulations is 100 h^{-1} Mpc except for SWH01, which uses 134 h^{-1} Mpc. The fourth column shows the number of two-dimensional maps which each simulation has created. The fifth column shows the field-of-view of the simulated two-dimensional maps. Note that RKSP00 and RT00 have not created two-dimensional maps, but computed the SZ angular power spectrum from the three-dimensional SZ power spectrum. The sixth−eighth columns show the cosmological parameters which each simulation uses. All the simulations use $\Omega_\Lambda = 1 - \Omega_{\rm m}$, and $n = 1.0$. The rightmost column shows references for the simulations.

Label	Code	$N_{\rm grid}$ or $N_{\rm sph}$	$N_{\rm map}$	F.O.V.	$\Omega_{\rm m}$	$\Omega_{\rm b}$	h	σ_8	Reference
RKSP00	MMH	128^3	—	—	0.37	0.049	0.7	0.8	Refregier et al. (2000)
SBP01	MMH	256^3	12	$2^\circ \times 2^\circ$	0.37	0.049	0.7	0.8	Seljak, Burwell, & Pen (2001)
SWH01	GADGET	224^3	15	$1^\circ \times 1^\circ$	0.3	0.04	0.67	0.9	Springel, White, & Hernquist (2001)
daSilva01	HYDRA	160^3	30	$1^\circ \times 1^\circ$	0.35	0.0377	0.71	0.9	da Silva et al. (2001b)
RT00	RAMSES	256^3	—	—	0.3	0.039	0.7	0.93	Refregier & Teyssier (2000)
ZPW02	MMH	512^3	40	$1\overset{\circ}{.}19 \times 1\overset{\circ}{.}19$	0.37	0.05	0.7	1.0	Zhang, Pen, & Wang (2002)

APPENDIX A: GAS POLYTROPIC INDEX

In this appendix we derive an exact formula for the gas polytropic index γ and give fitting formulae for γ and for the mass–central temperature normalization factor, $\eta(0)$ (see equation 19 for definition).

We specify γ and $\eta(0)$ uniquely by requiring that the gas-density profile, $\rho_{\rm gas}(x)$, matches the dark-matter density profile, $\rho_{\rm dm}(x)$, in outer parts of the haloes. We do this by solving the following equation,

$$s_* \equiv \left.\frac{d\ln\rho_{\rm gas}(x)}{d\ln x}\right|_{x=x_*} = \left.\frac{d\ln\rho_{\rm dm}(x)}{d\ln x}\right|_{x=x_*}, \tag{A1}$$

where s_* denotes a slope of the dark-matter density profile at a matching radius x_*.

In previous paper (Komatsu & Seljak 2001) we have shown that equation (A1) determines $\eta(0)$ uniquely for a given γ,

$$\begin{aligned}\eta(0) \quad = \quad & \gamma^{-1}\left\{\left(\frac{-3}{s_*}\right)\left[\frac{x_*^{-1}m(x_*)}{c^{-1}m(c)}\right]\right.\\ & \left. +3(\gamma-1)\left[\frac{c}{m(c)}\right]\int_0^{x_*}du\frac{m(u)}{u^2}\right\}, \end{aligned} \tag{A2}$$

where $m(x)$ is a non-dimensional dark-matter mass profile defined by

$$m(x) \equiv \rho_{\rm s}^{-1}\int_0^x du\, u^2\rho_{\rm dm}(u), \tag{A3}$$

and $\rho_{\rm s}$ is a scale density. Equation (A2) makes the matching condition, equation (A1), satisfied at radius x_*.

Next, we require that $\eta(0)$ does not depend upon a particular choice of x_*; this requirement specifies γ uniquely. While we have done this by finding an empirical fitting formula for γ in the previous paper (equation 25 of Komatsu & Seljak 2001), we derive here an exact formula for γ by solving the following equation,

$$\left.\frac{\partial\eta(0)}{\partial x_*}\right|_{x_*=c} = 0, \tag{A4}$$

where c is the concentration parameter (see equation 10 for definition). This equation means that $\eta(0)$ normalization does not depend upon the particular choice of x_*.

We find that equation (A4) gives γ as a function of c,

$$\gamma = 1 - \left.\frac{1}{s_*}\right|_{x_*=c} + \left.\frac{\partial\ln\left[m(x_*)/s_*\right]}{s_*\partial\ln x_*}\right|_{x_*=c}. \tag{A5}$$

This formula gives the polytropic index of gas in haloes with any given dark-matter density profiles.

Hereafter, we evaluate γ and $\eta(0)$ for the NFW profile (Navarro, Frenk, & White 1997), $\rho_{\rm dm}(x) = \rho_{\rm s}x^{-1}(1+x)^{-2}$. We find

$$s_* = -\frac{1+3x_*}{1+x_*}, \tag{A6}$$

and

$$m(x) = \ln(1+x) - \frac{x}{1+x}. \tag{A7}$$

By substituting s_* and $m(x)$ into equation (A5), we obtain γ. We then substitute s_*, $m(x)$, and the derived γ into (A2) to obtain $\eta(0)$.

The upper panel of figure A1 shows γ as a function of c compared to the fitting formula in equation (17). For comparison, the figure also plots the fitting formula which we have given for $4 < c < 11$ in Komatsu & Seljak (2001). The new formula, equation (17), is valid for $1 < c < 25$.

By substituting γ from equation (A5) into equation (A2) we obtain $\eta(0)$ as a function of c. The bottom panel of figure A1 shows $\eta(0)$ as a function of c and also the fitting formula $\eta(0)$ in equation (18). For comparison, the figure also plots the fitting formula given in Komatsu & Seljak (2001).

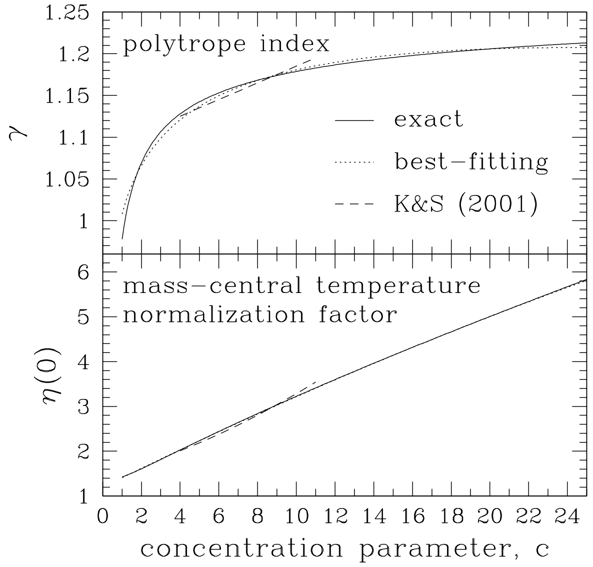

Figure A1. The top panel shows the polytropic index of gas in haloes, γ, while the bottom panel shows the mass–central temperature normalization factor, $\eta(0)$ (see equation 19 for definition), as a function of the concentration parameter c. The solid lines plot exact values calculated from equation (A5) and (A2) for γ and $\eta(0)$, respectively. The dotted lines plot the best-fitting formulae, equation (17) and (18) for γ and $\eta(0)$, respectively. The dashed lines plot the fitting formulae given in Komatsu & Seljak (2001) for $4 < c < 11$.